Construction of a sandwich-like Gr/Ni composite coating on AZ91D magnesium alloy to achieve excellent corrosion and wear resistances in the seawater

Bingdong Qin[1,2], Liqiu Ma[1,*], Shuncai Wang[3], Chunju Hou, Shengguo Zhou[2,*]

[1] *School of Science, Jiangxi University of Science and Technology, Ganzhou 341000, PR China*

[2] *School of Materials Science and Engineering, Jiangxi University of Science and Technology, Ganzhou 341000, PR China*

[3] *national Centre for Advanced Tribology at Southampton (nCATS), School of Engineering Sciences, University of Southampton, SO17 1BJ, UK*

Abstract: Preventing AZ91D magnesium alloy from severely wear and corrosion should be of significance so as to extend its applications. In this work, we systemically investigated graphene (Gr) doping concentration to influence the structure and performance of Gr/Ni composite coatings on AZ91D Mg alloy in the seawater. The results showed that the optimal Gr doping Gr/Ni composite coating on Mg alloy could possess much higher hardness and better adhesive strength as well as much lower wear rate in the seawater. Moreover, the novel composite sandwich structure was utilized to construct multi-interfacial Gr/Ni composite coating on AZ91D Mg alloy, which successfully achieved much more excellent long-term corrosion and wear resistances in the marine. Density functional theory calculations clarified the mechanism of sequential adsorption of nickel to graphene, indicating that it easily gave rise to graphene agglomeration in electroplating process. However, the multi-interfaces could provide more stretching space for graphene sheets and reduce the folding tendency of graphene. These results indicated that

* Correspondence author. Tel.: +86 18070470830. E-mail: malq@jxust.edu.cn

the sandwich-like structure Gr/Ni composite coating brought excellent properties for AZ91D magnesium alloy to enhance its services in the marine and aviation environments.

Keyword: AZ91D, Graphene/Ni, Sandwich-like, Corrosion

1.Introduction：

As we know, AZ91D magnesium alloy has excellent characteristics of low density, good thermal conductivity, strong anti-electromagnetic interference, easy casting, and convenient recycling [1-3]. Therefore, AZ91D magnesium alloys is widely used in portable microelectronic, automotive industry, biodegradable materials, and aviation. Nevertheless, AZ91D magnesium alloy application scopes were hampered by high chemical activity and high wear rate defects from itself. Especially in some harsh environments, such as the containing Cl^- and marine environment, the magnesium alloy surface would exhibit honeycomb and a large amount of white hydroxide sediment. In addition, under the state of tensile stress, the rate of formation of loose oxides on the surface of magnesium alloys is accelerated, resulting in high stress corrosion defects. Hence, it is particularly important to use coating protection on the surface of magnesium alloys to solve its defects problem. These modification schemes include magnetron sputtering, anodic oxidation, micro-arc oxidation, chemical conversion coating, electrodeposition, and organic coating [4,5]. Electroplating coating allows to the subsequent deposition of other metals by means of metallurgical bonding. Therefore, electroplating is a very effective process to improve magnesium alloy service performance. And, the electroplating coating can preserve the low resistance and excellent electromagnetic shielding properties of magnesium alloys to the greatest extent. In the industrial production, the common metal coatings on AZ91D are copper, zinc and nickel coatings,

and Ni coating is a common option as a protective or pre-plating coating for the magnesium alloy. The potential between Ni coating and Mg alloy substrate is lower than that of cyanide copper plated on substrate. Therefore, this combination of Ni coating and Mg could reduce the corrosion rate of the layers. Moreover, the pure Ni coating could have some advantages of strong bonding and non-toxicity with Mg alloy.

Unfortunately, the hydrophilicity of pure nickel coatings makes them vulnerable to damage by corrosive media, which reduces their protective effect for AZ91D. Through numerous studies, researchers found that the nanoparticles doping into the nickel coating could improve the hardness, anti-wear properties, corrosion resistance and lubricity of the coatings [6,7]. During the electrodeposition process, the nanoparticles suspended in solution transport, absorb and co-deposit with Ni^+ into deposits. Commonly adding particles for nickel-based composite coatings included: SiO_2, SiC, TiN etc. As a new derivative of graphene, graphene oxide (GO) owns good mechanical properties, a prominent aspect ratio, and strong barrier performance. In addition, GO includes oxygen containing functional groups, which is beneficial for application and modification in surface engineering [8]. The hydrophilicity of GO enhances its dispersion in the electrolyte so as to facilitate to plate the graphene/Ni composite coating. Kurapova et al. [9] used the powder metallurgy process to prepare bulk nickel-graphene composites with relatively higher hardness and tensile strength. Askarnia et al. [10] used electrophoretic deposition technology to prepare alumina/GO coating on AZ91D magnesium alloy, and it found that the optimal GO was beneficial to improve the hardness, the bond strength and corrosion resistance of the coating.

Although the technology of preparing composite coatings is relatively mature on the surface of magnesium alloys, its long-term corrosion resistance is still unsatisfactory. Some researchers reached the

long-term corrosion resistance of the coating by the multilayer structure, which was virtue of the excellent interfacial effect possessed. P. Bagalà et al.[11] prepared CeO_2/stannate multi-layer films on the surface of AZ91D magnesium alloy by chemical conversion method and sol-gel impregnation method. Electrochemical results show that the multi-layer structure can significantly improve the long-term corrosion resistance of magnesium alloys. Zhang et al.[12] deposited a hafnium monolayer and a Hf/Si_3N_4 multilayer film on the surface of AZ91D magnesium alloy by magnetron sputtering. This study shows that multi-layer coatings can delay the intrusion of corrosive media. However, there were few reports on the realization of graphene/Ni multilayer composite coating on AZ91D magnesium alloy by electroplating process. At the same time, the explanations of most studies on the agglomeration of graphene sheets are not very convincing.

Firstly, this study investigated the effect of doping graphene with different contents on the surface structure of graphene/Ni composite coatings. Then, the effects of different contents on the properties of composite coatings were systematically studied from the aspects of mechanical properties, tribological behavior in the atmospheric and marine environment, electrochemical tests. Especially, the composite coating with optimal graphene was used to combine with the synergetic multi-interface structure so as to construct a sandwich-like Gr/Ni composite coating on the surface of AZ91D magnesium alloy. It was found that the multi-interface structure can reduce the agglomeration defects of graphene. Finally, we used first-principles calculations to explain the irreversible agglomeration phenomenon of graphene from the adsorption characteristics of graphene on nickel in the electroplating process. This study was expected to clarify the mechanism of graphene and multi-interface synergism for sandwich-like Gr/Ni composite coating,

which could also provide a feasible way to protect AZ91D magnesium alloy to enhance its services in marine and aviation environments.

2. Experimental

2.1 Pre-treatment process of Mg alloy substrates

The selecting experimental substrates were the commercial AZ91D alloys, and the size of Mg alloy was controlled at 20×15×5 mm (Dongguan Kuanyu Metal Co., Ltd.). All Mg alloy substrates were firstly sanded, and then polished with the order of 320, 600, 1200 size sandpaper until there were no obvious sanding marks on the surface. After grinding, the Mg alloys were placed in ethanol solution and ultrasonically cleaned for 60 minutes, and the purity grades of chemical reagents were analytical purity in the experiments. The key pre-treatment process to Mg alloy substrate included as following steps: (1) Alkaline washing: The ultrasonically cleaned samples were suspended and immersed in the alkaline washing solution, and treated at a constant temperature of 65 ℃ with stirring for 30 min. (2) Pickling: The samples after alkaline washing were immersed in acid washing solution at room temperature for 15 s. (3) Activation: The acid-washed samples were immersed in the activation solution and treated at 75 ℃ for 30 minutes. (4) Activation cooling: After the activation is completed, the sample is placed in the activation solution at room temperature to cool for 0.5 minute. The sample was immersed into cooling water, after the activation, which resulted in the exfoliated risk of fluoride film. The reason was that the fluoride film had not obtained repair from activation solution, which could accelerate the corrosion in the layers. The fluorinated film formed by activation was very unstable, and it was easy to be damaged when it is directly cooled in the water. It must be cooled with an activation liquid before performing

next step. (5) Zinc pre-treatment: After activation and cooling, the samples were suspended and immersed in the immersion zinc solution, kept at 75 ℃ and stirred for 30 minutes. The purpose of stirring is to increase the concentration of zinc ions in the zinc immersion solution and avoid delamination. The detail parameters of pre-processing steps to Mg alloys were as also listed in Table 1. Between each step in pre-treatment process, the surface of Mg alloys was cleaned with distilled water to prevent residual liquid contamination.

Table 1. The composition of the solvent on pre-treatment process.

Process operation	**Solution Composition (AR)**	**Concentration**
Ultrasonic cleaning solution	Absolute Ethanol	———
Alkaline cleaning solution	Na_2CO_3 $Na_3PO_4{\cdot}12H_2O$ $Na_2SiO_3{\cdot}9H_2O$ OP emulsifier	40 g/L 24 g/L 47 g/L 3 ml/L
Acid pickling solution	HNO_3 (68%) H_3PO_4 (85%)	6 ml/L 120 ml/L
Activation solution	$K_4P_2O_7$ Na_2CO_3 KF H_3PO_4 (85%)	66 g/L 15 g/L 3.7 g/L 25 mL/L
Zinc dipping solution	$K_4P_2O_7$ Na_2CO_3 LiF $ZnSO_4{\cdot}7H_2O$	150 g/L 5 g/L 11 g/L 56 g/L

2.2 Coating depositions

The nickel plate (1.5×0.5×20 cm) was used as the anode and graphite as the conducting electrode (1.5×0.5×20 cm) as the cathode. The galvanized magnesium alloy sample was installed on the graphite cathode, waiting for electroplating. The spacing between the sample and the anode

was controlled at 3 cm. The water bath temperature was 45 ˚C and the magnetic stirrer speed was 400 rpm/min. In the experimental process, the current density of the electroplating power supply was maintained at 4 A/dm^2 for the pure Ni coating and Ni transition layer, where the as-deposited nickel layer had the lowest porosity. Herein, the time of electroplating pure nickel on Mg alloy must be controlled by 30 min.

The electroplating process of the graphene/nickel composite coating was shown in Fig. 1. Preparation process of electroplating solution for composite coating was listed in Table 2. The graphene sheets specification selected a single-layer nanosheets with a width about 200-400 nm and the length about 1 μm. The plating solution needs to be ultrasonically dispersed for 2 hours, and then the plating solution was placed in a constant temperature water bath for continuous stirring for 0.5 hours. The above operation was to improve the uniform dispersion state of graphene sheets in the plating solution. The electrode plate spacing was controlled at 5 cm. The plating solution temperature was 45 C° and the rotational speed was 800 rpm/min. The high rotating speed and large spacing during the preparation process could effectively decline the aggregation of graphene into the coating. The electroplating Gr/Ni coating time spent 30 min. Subsequently, a series of graphene/Ni composite coatings with five different doping contents were electroplated on the Mg alloys substrate where the graphene doping concentrations were 0.05 g/L, 0.1 g/L, 0.2 g/L, 0.3 g/L and 0.4 g/L, respectively, and these samples were nominated by Gr/Ni-1, Gr/Ni-2, Gr/Ni-3, Gr/Ni-4 and Gr/Ni-5, respectively.

Table 2. Electrodepositing process of pure Ni and grapheme/Ni composite coatings

Process operation	**Solution composition**	**Concentration**
Ni electrodepositing	$NiSO_4 \cdot 6\ H_2O$	120 g/L
	NH_4HF_2	40 g/L
	$NH_3 \cdot H_2O$	40 mL/L
	$C_6H_5O_7$	10 g/L
	$(NH_4)_3C_7H_4NO_3SNa$	3 g/L
	SDS	0.1 g/L
Grapheme/Ni electrodepositing	$Ni(NH_2SO_3)_2$	310 g/L
	H_3BO_3	40 g/L
	$NiCl_2 \cdot 6H_2O$	8 g/L
	GO nanosheets	0.05,0.1,0.2,0.3,0.4 g/L

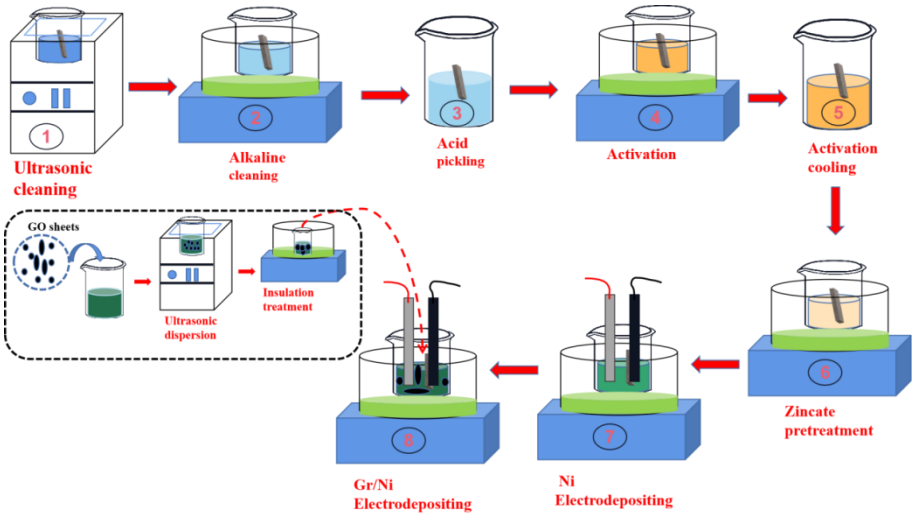

Fig. 1. Schematic of electroplating process for the Gr/Ni coatings.

In addition, the $Ni(NH_2SO_3)_2 \cdot 4H_2O$ plating solution with a graphene concentration of 0.2 g/L was selected to prepare a double-layer composite coating. The pure nickel coating was applied to the transition layer for the composite graphene/nickel coating. The deposition time of each step is

changed to be 15 min. The two coatings are alternately deposited twice, and the total deposition time is 60 min. The purpose of controlling the total deposition time is to ensure that the thickness of the composite coating is basically the same, which is convenient for subsequent physical and chemical analysis.

2.3 Characterization of coatings

Scanning electron microscope (SEM) equipment was used to analyze the cross-section and surface morphology of as-plating Gr/Ni composite coatings, and X-ray diffraction (XRD) was performed to analyze their phase composition and grain size. JY-82A contact angle test instrument was to analyze the change of contact angle of coating surfaces. The BY-2000 device was used to analyze the variation of the roughness of the coating surface, which can provide supporting evidence for the wear mechanism of the coating and the variation of the contact angle. The tribological behavior of the coating was analyzed by a linear reciprocating tribometer. The variation of the abrasion marks was analyzed with the aid of a three-dimensional profiler, and SEM was used to further characterize the coating wear mechanism. Raman spectroscopy was used to analysis the graphene in the composite coating. At last, the electrochemical workstation was investigated to the corrosion resistance for the coatings via immersion in 3.5. wt% NaCl solution for different duration. The sample of exposure area was set of working electrode, the calomel electrode was the reference electrode and platinum plate was the counter electrode. Those constituted the three electrode system. EIS measurement setup: the sinusoidal signal amplitude was 5 mV, and the measurement frequency range was 100 kHz to 0.01 Hz in room temperature.

2.4 Calculation method and model

All calculations in this study were performed using DFT-based first-principles calculations. All calculations were performed using the VASP software with a cutoff energy of 550 eV and using the Perdew Burke Ernzerhof parameterization (PBE) generalized gradient approximation (GGA) [13,14]. The self-consistent cycle is repeated until the total energy difference is less than 10^{-5} eV and the force acting on the atoms is less than 0.01 eV/Å. Optimization of atomic positions using the conjugate gradient method.

3. Results and discussion

3.1 Microstructure and composition of Gr/Ni composite coatings

The SEM and AFM images of surface morphologies for as-plating graphene/Ni composite coatings on Mg alloy substrate with five different graphene sheet content are shown in Fig. 2 (a-e). The Fig. 2(a) could be seen that there was exhibited scale-like feature and a wrinkle feature for Gr/Ni-1 coating, which might be attributed to a raised structure on Mg alloy surface caused by the micro etching action of pretreatment solution. The SEM surface morphologies further revealed that the cauliflower-like surface structure gradually became much more apparent to as-plating Gr/Ni composite coatings as the increase of graphene sheet doping concentration. This phenomenon might be caused by the micro-nano electrode effect formed during the embedding of the graphene sheet [15]. The Ni^{+} would preferentially reduce the location on the Gr sheets, the reason was the electrical conductivity of Gr sheets. Consequently, a large number of grain-shaped nucleation growth networks were formed in the microelectrode region to cause a large cauliflower-like structure for the surface of Gr/Ni composite coating as the increase of added graphene sheets. Most importantly, the functional groups containing oxygen on

graphene nanosheets had strong adsorption effect on Ni^{+}, which would promote the co-reduction process of Ni and graphene sheets [16]. With increasing the dopant concentration, the Gr/Ni-4 and Gr/Ni-5 samples exhibited large-sized unit cell features. The result may be due to irreversible agglomeration defects during graphene reduction, which reduces the size of micro-nano electrodes, resulting in faster nickel growth than nucleation [16,17]. The inset of Fig. 2 showed the AFM images of the surface three-dimensional morphologies of the Gr/Ni composite coatings, and the calculated average surface roughness (Ra) of the Gr/Ni-1, Gr/Ni-2, Gr/Ni-3, Gr/Ni-4, and Gr/Ni-5 nickel composite coatings were 51.1, 59.7, 65.9, 76.8, and 89.4 nm, respectively. The amount of graphene doping was positively correlated with the surface roughness of the coating, which was consistent with the SEM observations for Gr/Ni composite coatings.

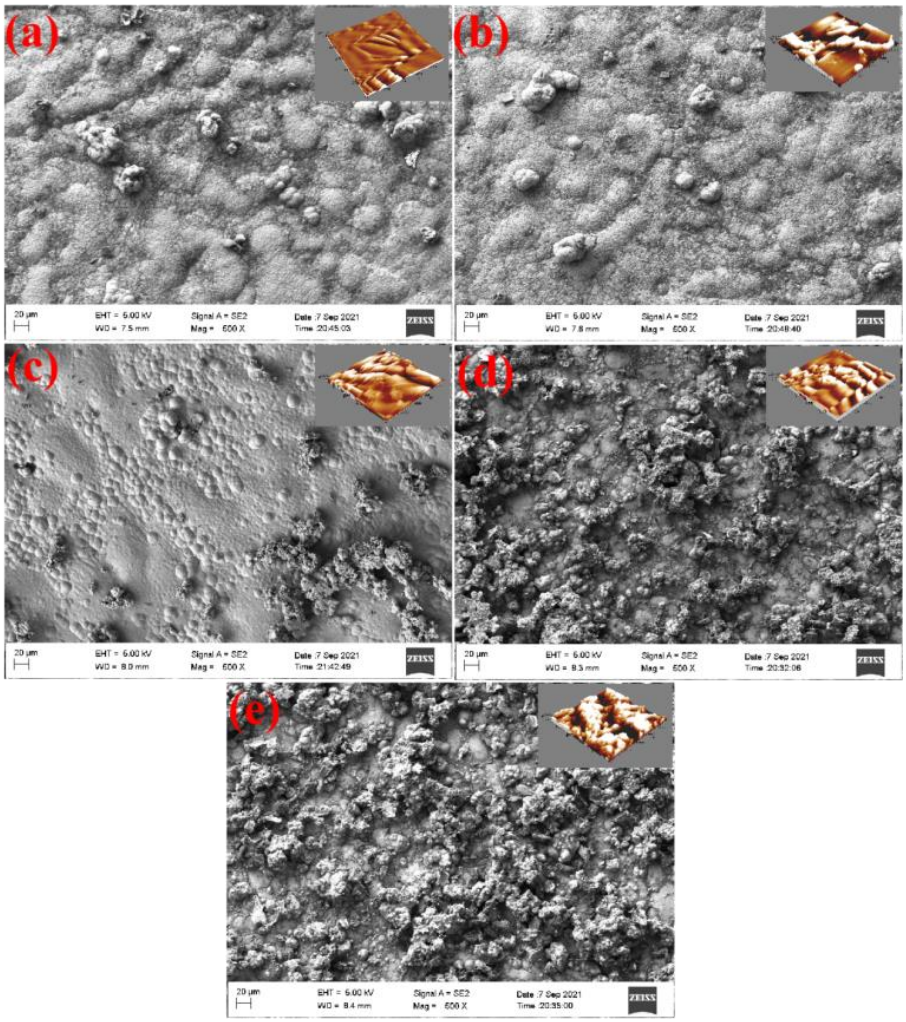

Fig. 2. SEM surface morphology images and AFM of Gr/Ni composite coatings: (a) Gr/Ni-1; (b) Gr/Ni-2; (c) Gr/Ni-3; (d) Gr/Ni-4; (e) Gr/Ni-5.

Fig. 3 presents the XRD patterns of different Gr/Ni composite coatings, it could be seen that the 2θ diffraction peaks at 44°, 52° and 76° correspond to the (111), (200) and (220) crystalline planes of face centered cubic nickel, respectively. The Gr/Ni-1 coating exhibited the highest diffraction peak at the position of 52°, indicating that the corresponding crystal orientation was the best crystal plane for growth. In general, (200) is the dominant crystal growth direction for pure nickel coatings with low hardness and high ductility, and (111) is the high hardness characteristic of nickel coatings [7]. With increasing doping graphene content, the diffraction peaks were altered for the as-plating

Gr/Ni composite coatings. The diffraction peak of Gr/Ni-3 at (111) presented a close intensity of diffraction peak at (200), indicating that it might possess a relatively higher hardness Gr/Ni-3 composite coating, which was also confirmed by a later hardness test. The diffraction peak of the (111) plane of Gr/Ni-5 started to be lower than that of the (200) plane, which would be mainly due to aggregation defects by high graphene doping content and graphite agglomeration. The above results indicated that the doping content of graphene sheets should select the optimum so that it could give rise to a shift in the direction of high extension. In addition, the grain size of the coating was roughly calculated by Scherrer's formula, so as to analyze the grain refinement effect of the doping content in the Gr/Ni composite coating. The average grain sizes of Gr/Ni-1, Gr/Ni-2, Gr/Ni-3, Gr/Ni-4 and Gr/Ni-5 were calculated to 106, 100, 97, 112, 120 nm, respectively. It found that the grain size firstly decreased and then increased with increasing graphene doping concentration for Gr/Ni composite coating. The micro-nano electrode effect of graphene sheets could accelerate the nucleation of nickel so that it could promote grain refinement at optimum graphene doping content for Gr/Ni composite coating. When the graphene doping concentration was more than 0.2 g/L, the agglomeration defect of graphene could change the growth characteristics of nickel in the extension direction. The phenomenon was because of the reduction reaction of GO to pristine Gr. The higher defect scope of agglomeration usually included an abundant of oxygen-containing functional group. GO is better than Ni+ for capturing e^+ capacity, which disturbed the Ni^+ reduce process. The more oxygen-containing groups should be the more favorable the graphene oxide reduction reaction. Besides, the agglomeration defect is proportional to oxygen-containing groups. Consequently, the agglomeration defect will result in a lower grain nucleation rate of Ni

than the grain growth rate [17-20]. Therefore, the Gr/Ni-4 and Gr/Ni-5 samples could exhibit a coarsening grain. XRD test shows that the composite coating prepared by doping 0.2 g/L graphene has the smallest grain size, and the grain refinement is beneficial to improve the hardness of the coating.

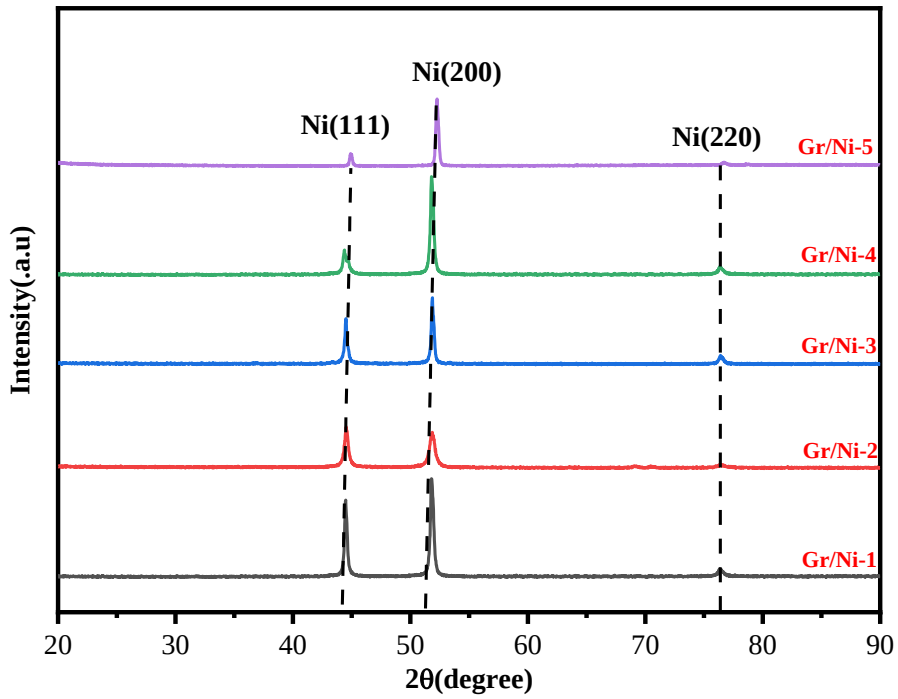

Fig. 3. XRD patterns of different Gr/Ni composite coatings.

Raman spectroscopy could effectively analyze the existing state of graphene inside the coating. Fig. 4 showed the Raman spectra of graphene diffraction peaks in the composite coatings with different concentrations. The characteristic peaks of graphene were the D and G peaks corresponding to 1345 cm^{-1} and 1595 cm^{-1}, respectively. After a Gaussian fit to the Raman spectrum of the composite coating, the I_D/I_G values of the two peak intensities were obtained. The I_D/I_G values of Gr/Ni-1, Gr/Ni-2 and Gr/Ni-3 samples were 1.23, 1.11 and 1.02, respectively. The reversal of the D and G peaks in the coating gradually decreased [17], indicating that the defects in the reduced graphene were

reduced. It could be due to the co-reduction synergistic effect of graphene and nickel at appropriate doping concentrations reducing the structural defects of graphene distortion and deformation. However, the I_D/I_G values of the Gr/Ni-4 and Gr/Ni-5 samples were 1.21 and 1.62, respectively. It was because the reduction of graphene was more active at high doping concentration, thus weakening the synergistic effect between graphene and nickel. In addition, the 2D characteristic peak (2700 cm^{-1}) was observed for the Gr/Ni-3 sample. The result demonstrated that the graphene agglomeration defect was reduced at this concentration and had superior graphene sheet properties. At the same time, it also provided evidence for the good corrosion resistance and friction resistance of the composite coating at this concentration.

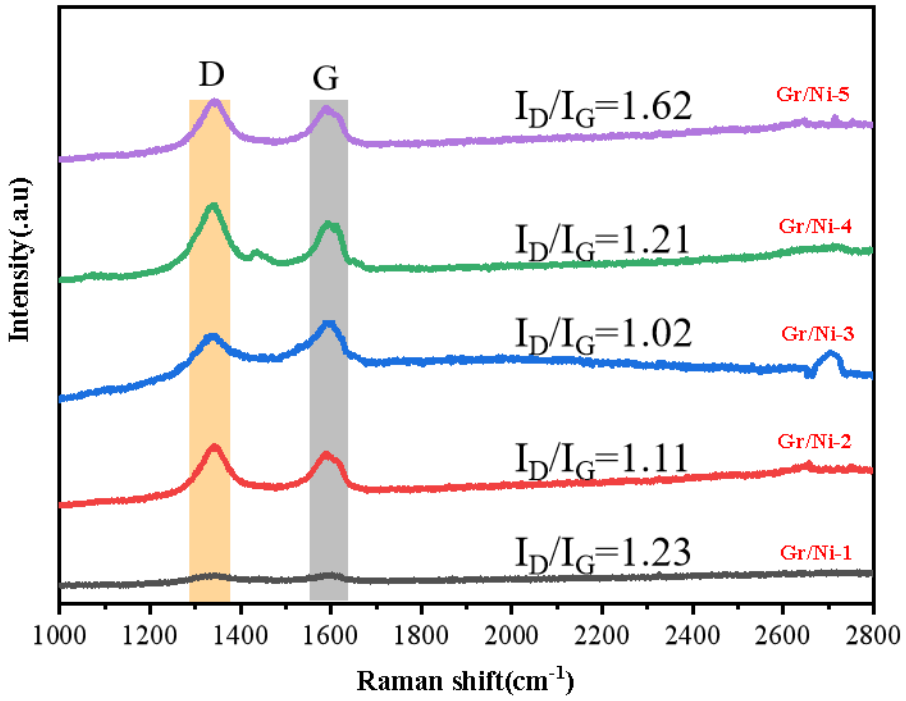

Fig. 4. Raman spectra of different Gr/Ni composite coatings.

Fig. 5 showed the image of SEM cross-sectional morphology of typical Gr/Ni-3 and its associated EDS data. It can be seen that the total thickness of as-plating Gr/Ni-3 composite coating was about 6 μm, which

could present two distinct layers of pure nickel transitional layer and graphene/Ni composite top layer. The Gr/Ni composite coating was embedded with many black micro-flake substance, which was a strong evidence that graphene was successfully deposited in the composite coating. The inset line scan data of the coating also demonstrated the presence of C element in as-plating Gr/Ni composite coating.

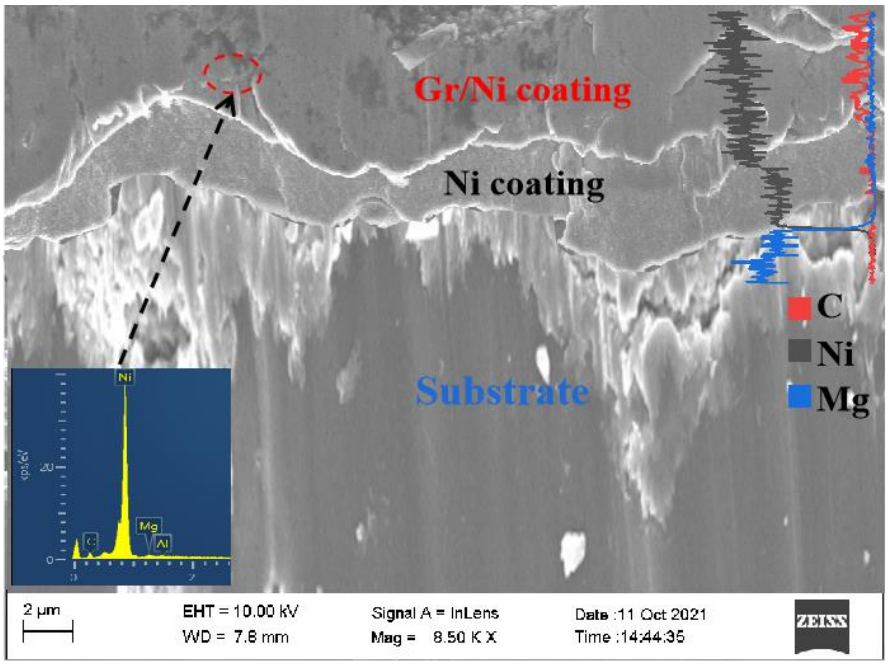

Fig. 5. SEM cross-sectional morphology of Gr/Ni-3 composite coating.

The static contact angle could quickly reflect the wetting properties of the coating surface [18,19]. It was well known that the smaller of water contact angle, the better the water-wetting performance of the surface, and vice versa, the better the hydrophobicity. In general, hydrophobic coatings had contact angles greater than 90 °. Fig. 6 (a) showed the water contact angle of all composite coatings. It could be seen that all coatings had contact angles greater than 100 ° and exhibited excellent hydrophobic properties. The contact angle of the Gr/Ni-3 coating increased to 131.1 °. With the help of Young-Dupre formula (1) and Wenzel's wetting equation [19-21] (2) for non-ideal solid surfaces, the mechanism of the contact angle

of the coating surface was explained (3).

$$W_{sl} = \sigma_{\mathrm{lg}} \times (1 + \cos\theta) \quad (1)$$

$$\cos\theta_r = r \times \cos\theta \quad (2)$$

$$\cos\theta_r = (W_{\mathrm{sl}} / \sigma_{\mathrm{lg}} - 1) \times \mathrm{r} \quad (3)$$

W_{sl} was the work of adhesion between solid-liquid surfaces, σ_{lg} was the surface tension between gas and liquid, θ was the theoretical contact angle, θ_r was the actual measured contact angle and r was the surface roughness($\geqq 1$). In the atmospheric environment, we assumed that the σ_{lg} surface tension was the same for all coatings to simplify the calculation. Therefore, the main influencing factors of coating wetting performance were adhesion work and surface roughness. For composite coatings, nickel was a typical wetting material, graphene was hydrophobic material [20-22], and the adhesion work was the result of the combined action of the two. The wettability test results showed that the graphene sheet effectively reduces the adhesion work on the surface of the nickel-based coating, and the adhesion work of the coating had a further downward trend with the increase of the doping amount. Therefore, the high surface roughness and low adhesion work of the composite coating was beneficial to increasing the water contact angle of the coating as the doping concentration increased. However, with the increasing doping concentration, the contact angle of the coating decreased from 131.1 ° to 121.5 °, which was mainly due to the high reduction defect graphene brought by the high concentration, which increased the adhesion work of the composite coating. The contact angle test proves that the Gr/Ni-3 composite coating had the best hydrophobic properties, which was beneficial to prevent the corrosive medium from invading the coating and improve the corrosion resistance of the coating.

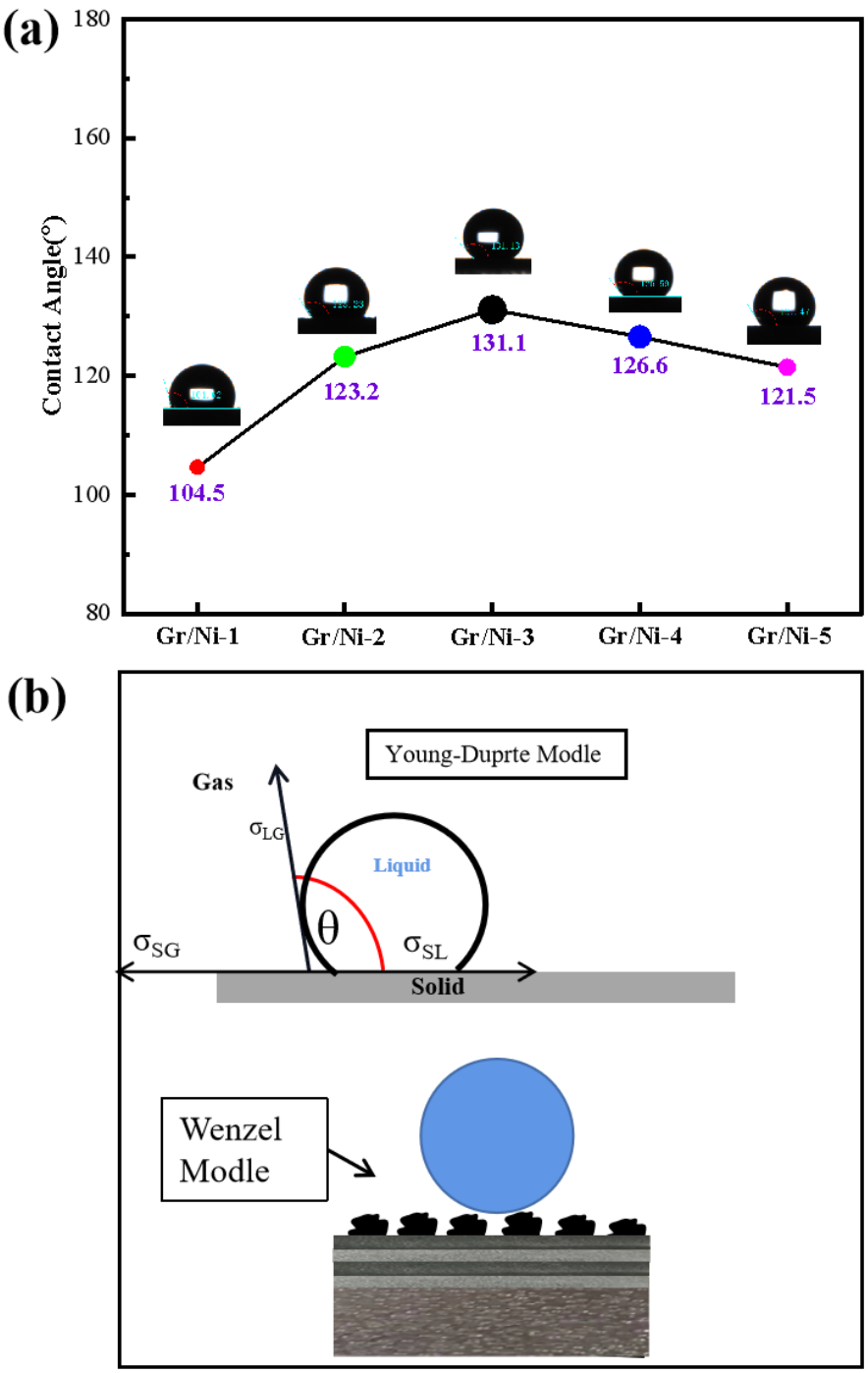

Fig. 6. Water contact angle on the surface of different Gr/Ni composite coatings (a) and the computational model diagram (b).

3.2 Microhardness and adhesive strength of Gr/Ni composite coatings

Fig. 7 showed the microhardness of Gr/Ni composite coatings prepared with different concentrations. The microhardness of the Gr/Ni-1,

Gr/Ni-2 and Gr/Ni-3 coatings were 640 HV, 763 HV and 983 HV, respectively. This could be explained from the following aspects: First, it could be known from the XRD results that the grain size of the composite coating decreases with the increase of graphene doping concentration. In general, a lower grain size could increase the hardness of the coating. Therefore, increasing the doping concentration could increase the hardness of the coating. Secondly, Cr nanosheets were strongly combined with the Ni matrix, which results improve dispersion strengthening effect. Jiang et al. had reported the GO nanosheets improve the hardness of substrate [23]. However, the microhardness of the Gr/Ni-4 and Gr/Ni-5 coatings decreased to 864 HV and 801 HV. It was because the increase in grain size reduces the effect of fine-grain strengthening. Meantime, the agglomeration tendency of graphene sheets increased, resulting in internal stress cracks and destroying the deformation resistance of the coating [25]. The hardness test results showed that the optimal doping concentration of graphene was 0.2 g/L, and the corresponding Gr/Ni-3 sample exhibited the highest microhardness, which was beneficial to wear resistance.

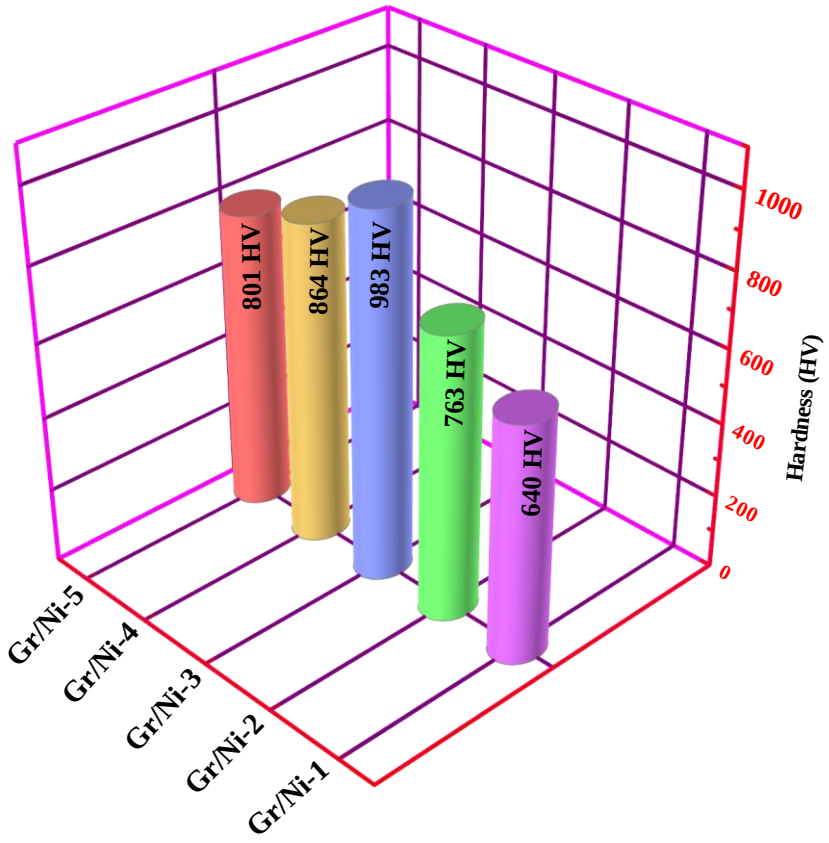

Fig. 7. Microhardness of different Gr/Ni composite coatings.

The scratch test, as shown in Fig. 8, reflected the bonding performances between as-plated coating and the substrate. In general, the high critical load (*Lc*) values correspond to high bonding properties between the coating and the substrate. The *Lc* of Gr/Ni-1, Gr/Ni-2 and Gr/Ni-3 coatings were 11 N, 14.6 N and 52.9 N, respectively. The results showed that the increase of graphene doping concentration was beneficial to improve the adhesion performance of the coating. The phenomenon could be explained from the perspective of the high hardness of the coating. The higher the hardness of the coating, the higher the normal load required when it is damaged by external force. Secondly, graphene sheets had a certain ability to hinder plastic deformation, thereby further delaying the occurrence of coating cracks. However, the *Lc* of Gr/Ni-4 and Gr/Ni-5 coatings were reduced to 33.4 N and 23.5 N. It was not only

related to the decrease in the microhardness of the coating, but also the increase of the distortion energy caused by the agglomeration of graphene inside the coating, which made the coating highly prone to stress cracks. The scratch test further proved that the Gr/Ni-3 composite coating prepared with the graphene content of 0.2 g/L could have the best mechanical properties.

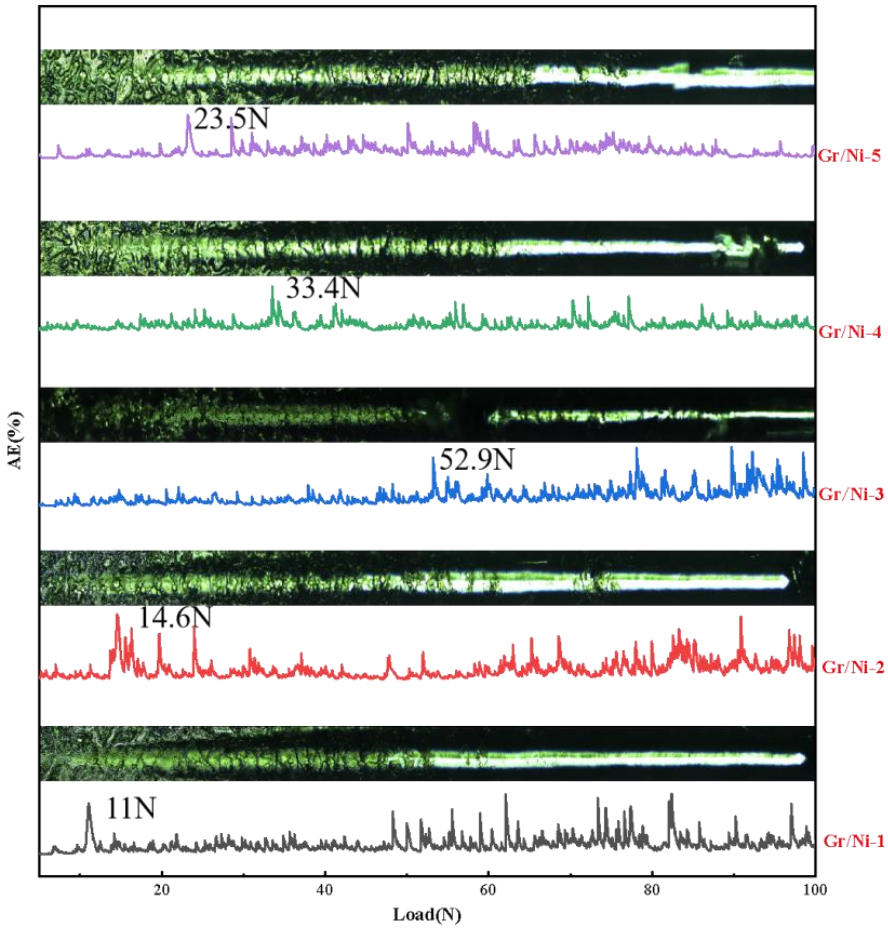

Fig. 8. Scratch acoustic emission curves and optical photographs of different Gr/Ni composite coatings.

3.3 Friction and wear behaviors of Gr/Ni composite coatings

Fig. 9 showed the friction coefficients of different Gr/Ni composite coatings under atmospheric conditions. The composite coatings friction coefficient decrease first and then rise with the increase of Gr doping

concentration. Compare with other coatings, the Gr/Ni-3 sample owned the lowest friction coefficient. The results showed that the Gr/Ni-3 coating had the best anti-friction performance, so 0.2 g/L graphene was the best doping concentration to improve the anti-friction performance of the composite coating. The phenomenon's main reason was that the excellent performance of Gr/Ni-3 coatings owned the highest hardness and excellent coating bonding properties, which could reduce plastic deformation during friction and improve their wear resistance. In particular, the strengthening effect and lubricating phase effect of graphene sheets could provide self-lubricating effect for the coating to reduce the wear effect. It is well known that the high hardness of the coating could resist wear damage [24]. The composite coating exhibits the highest hardness at 0.2g/L, so its wear resistance is stronger than other samples. At the same time, according to the Archard equation (4):

$$V = \mathrm{k}WS/(3H) \quad (4)$$

The k, V, S, W, and H respectively corresponds to the friction coefficient, wear volume, sliding distance, normal load, and hardness [23-26]. As showed in Fig. 10 (f), the specific wear rates of Gr/Ni-1, Gr/Ni-2, Gr/Ni-3, Gr/Ni-4, Gr/Ni-5 coatings were 4.1×10^{-5}, 3.7×10^{-5}, 3.5×10^{-5}, 3.6×10^{-5}, 3.7×10^{-5} $mm^3/(N\cdot m)$, respectively. The Gr/Ni-3 sample exhibited the lowest specific wear rate and the lowest friction coefficient, which indicates that the coating had the best anti-wear performance. Therefore, the Gr/Ni-3 composite coating was beneficial to improve the wear resistance of AZ91D magnesium alloy in the aviation environment.

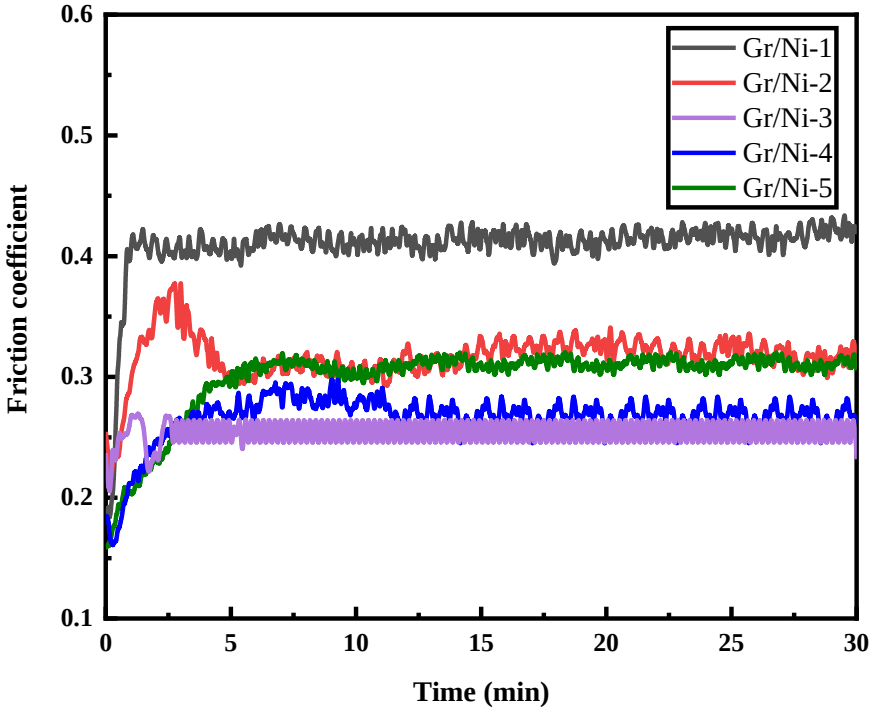

Fig. 9. The friction coefficient of different Gr/Ni composite coatings in atmospheric environment.

The 3D morphologies of all Gr/Ni coating wear scars were shown in Fig. 10 (a-e). The results showed that the Gr/Ni-3 sample owned the narrowest wear scar width of 300 μm and the shallowest depth of 4.5 μm. The wear scars of other composite coatings were all 400 μm wide and about 5μm deep. The surface of the wear scar was further characterized by SEM image, and the morphological characteristics of the wear scar are shown in Fig. 11 (a-e). The SEM images and the 3D wear scar images showed the same regularity: the wear scar features of the coating gradually become shallower and narrowed from Gr/Ni-1 to Gr/Ni-3, and then gradually widen to Gr/Ni-4 and Gr /Ni-5 finally reversed. In addition, the small sheets remaining in the coating indicated that the coating was mainly abrasive wear during the wear process, and the Gr/Ni-3 coating wears the least. The variation law of the surface wears scar morphology of the coating in the atmospheric environment was consistent with the

variation of the friction coefficient and wear rate, which further proved that the Gr/Ni coating prepared at 0.2 g/L has good wear resistance.

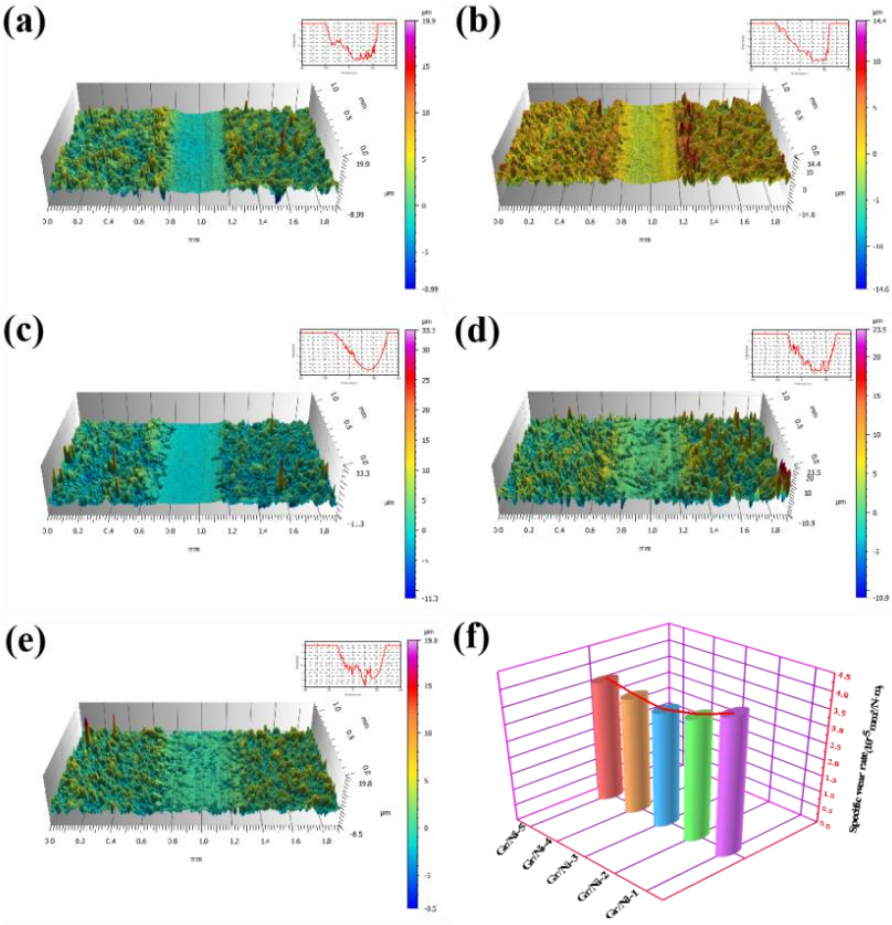

Fig. 10. The 3D images of wear tracks of Gr/Ni composite coatings in atmospheric environment: (a) Gr/Ni-1; (b) Gr/Ni-2; (c) Gr/Ni-3; (d) Gr/Ni-4; (e) Gr/Ni-5; (f) specific wear rate.

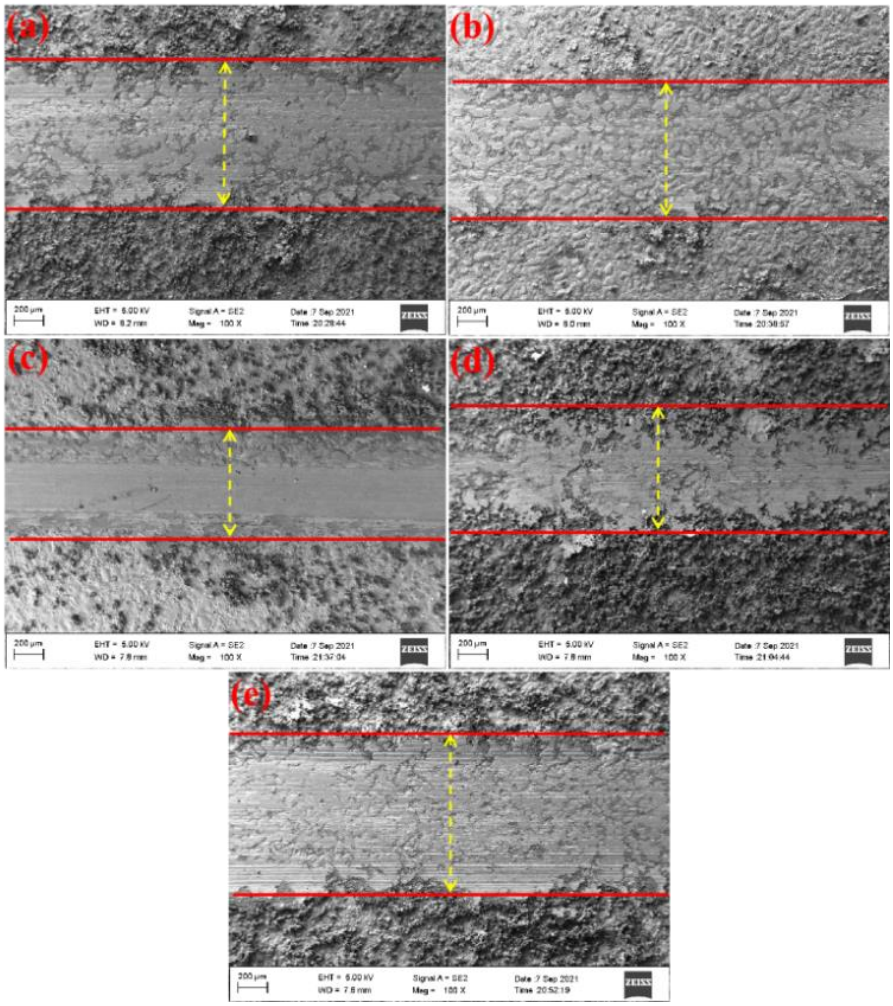

Fig. 11. SEM images of wear tracks of Gr/Ni composite coatings in atmospheric environment: (a) Gr/Ni-1; (b) Gr/Ni-2; (c) Gr/Ni-3; (d) Gr/Ni-4; (e) Gr/Ni-5.

Fig. 12 showed the friction coefficient of the composite coating in the seawater environment. The order of the friction coefficient was consistent with the change in the atmospheric environment. The Gr/Ni-3 coating had the lowest friction coefficient, which indicated that the composite coating at this concentration owned corrosion resistance under the seawater. Interestingly, the coefficient of friction of the composite coating in the seawater environment was lower than that measured in the atmospheric environment. It was mainly because seawater acts as a liquid lubricant in the friction process, reducing wear damage. The wear profile of Gr/Ni coatings was shown in Fig. 13 (a-e). The coating wear rate in

seawater environment was shown in Fig. 13(f). The wear rates of Gr/Ni-1, Gr/Ni-2, Gr/Ni-3, Gr/Ni-4, and Gr/Ni-5 were 3.4×10^{-5}, 2.9×10^{-5}, 2.5×10^{-5}, 2.8×10^{-5} and 2.9×10^{-5} $mm^3/(N\cdot m)$, respectively. The phenomenon was consistent with the change order of the friction coefficient, indicating that Gr/Ni-3 had the best wear resistance in the seawater environment. In particular, the SEM images of wear in a seawater environment (Fig. 14 (a-b)) exhibited corrosive wear characteristics. It was mainly due to the electrochemical reaction between the nickel in the coating and the free ions in seawater during the wear process, resulting in corrosive wear. The corrosion wears on the surface of the Gr/Ni-3 sample was the weakest, indicating that the composite coating prepared at this concentration could maximize the corrosion and wear resistance of magnesium alloys in the seawater environment. In summary, the composite coating prepared with doping concentration of 0.2g/L was the most beneficial to improve the wear resistance of AZ91D magnesium alloy in aviation and seawater environments.

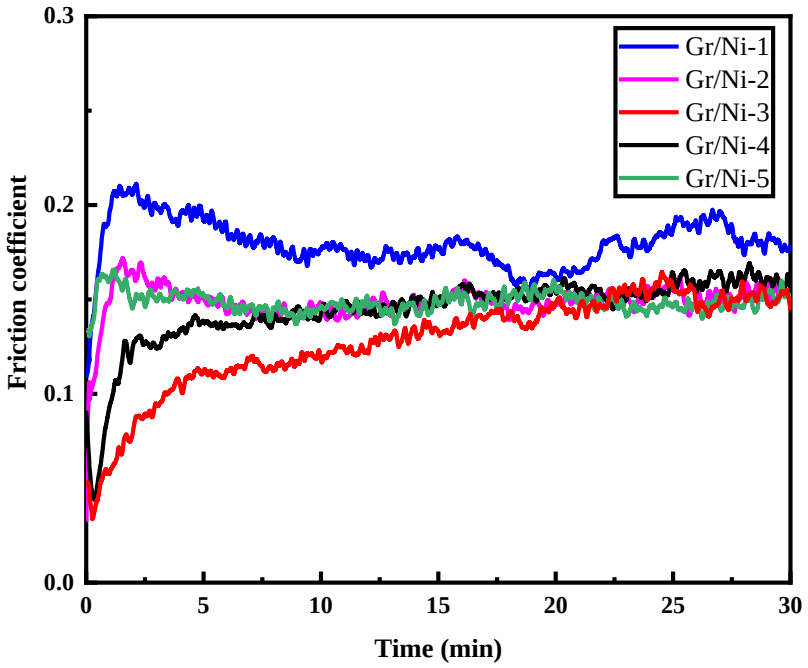

Fig. 12. The friction coefficient of different Gr/Ni composite coatings in artificial seawater environment.

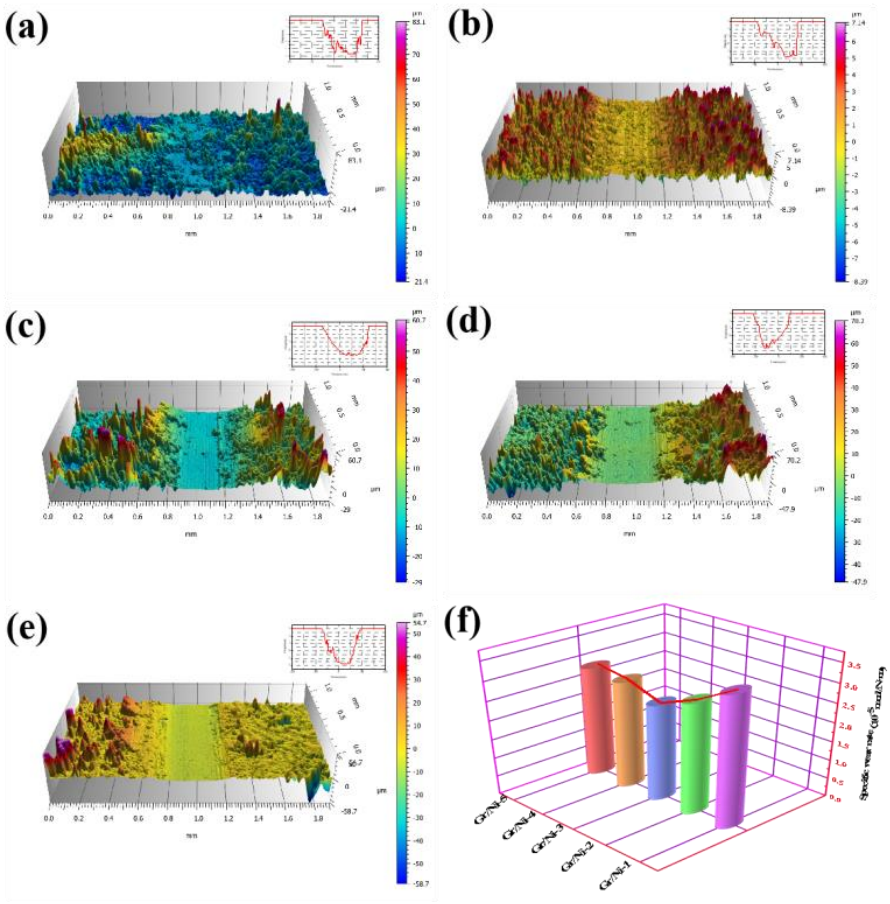

Fig. 13. The 3D images of wear tracks of Gr/Ni composite coatings in artificial seawater environment: (a) Gr/Ni-1; (b) Gr/Ni-2; (c) Gr/Ni-3; (d) Gr/Ni-4; (e) Gr/Ni-5; (f) specific wear rate.

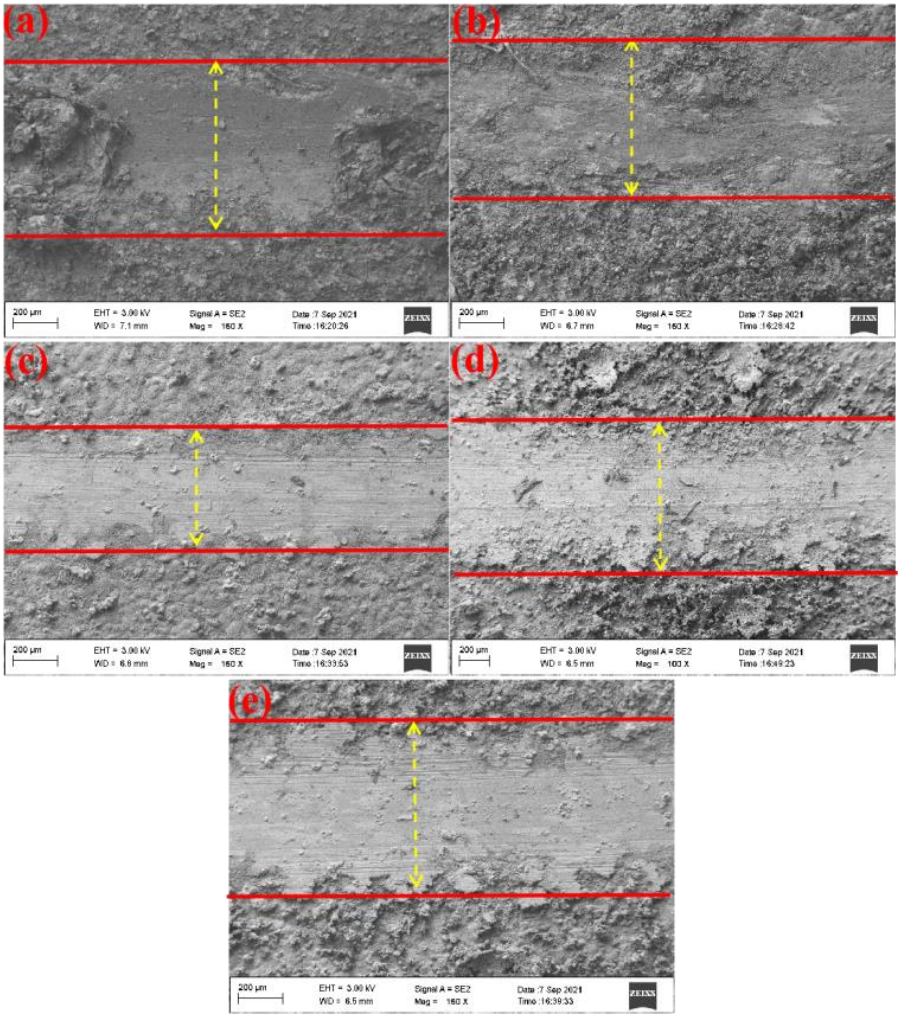

Fig. 14. SEM images of wear tracks of Gr/Ni composite coatings in artificial seawater environment: (a) Gr/Ni-1; (b) Gr/Ni-2; (c) Gr/Ni-3; (d) Gr/Ni-4; (e) Gr/Ni-5.

3.4 Corrosion resistances of Gr/Ni composite coatings

The corresponding electrochemical tests were performed after the coatings were immersed in 0.35 wt.% NaCl solution for 0.5 h. Fig. 15 (a) showed the potentiodynamic polarization curves of all composite coatings. It could be found that the Gr/Ni-3 exhibits the lowest corrosion current and the most positive corrosion potential. The results indicated that the composite coating prepared with 0.2 g/L graphene doping concentration had the best corrosion resistance. It could be explained from the following aspects: Firstly, during the corrosion process, Cl^- tends to be

adsorbed at the defects, thereby causing the corrosion effect. The micro-nano electrode effect brought by an appropriate amount of graphene doping is beneficial to reduce the grain size of the coating, thereby reducing the structural defects on the surface and reducing the porosity of the coating. Secondly, the low-defect reduced graphene sheet acts as the strengthening phase of the nickel-based coating, which improves the hydrophobicity of the coating surface and reduces the ability of the corrosive medium to wet the nickel layer [15-17]. Lastly, graphene would prevent Cl^- from passing through the surface of the coating, reducing the erosive effect of the corrosive medium on the coating. Therefore, the Gr/Ni-3 sample exhibits excellent corrosion resistance.

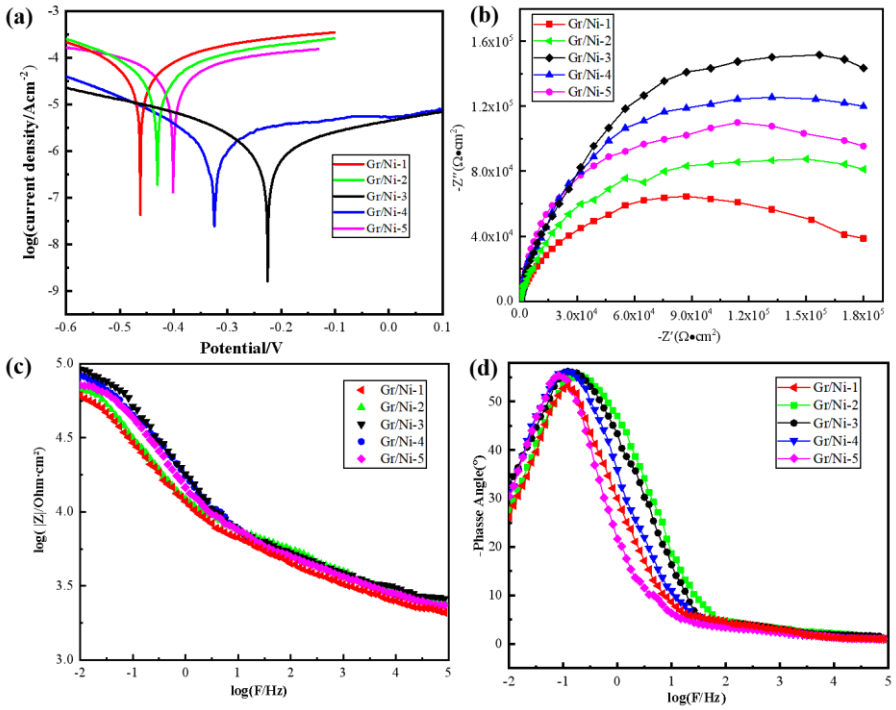

Fig. 15. The polarization curves of Gr/Ni composite coatings were immersed in 3.5wt.% NaCl solution for 30 min: (a) potentiodynamic curves, (b) EIS, (c) impedance modulus, (d) phase angle.

Fig. 15 (b) was the EIS spectrum of the composite coating. As we all

know, the larger the diameter of the capacitive arcs of EIS, the higher the corrosion resistance. Fig. 15(c) and (d) represent the impedance modulus and phase angle changes of the composite coating, respectively. Generally, the larger the impedance modulus or the higher the phase angle of the coating in the low frequency region, the stronger its passivating ability and the less likely it is to corrode [24-27]. It could be seen that Gr/Ni-3 sample exhibited the largest capacitive arcs diameter, the largest impedance modulus and the highest phase angle in the low frequency region. The result showed that the composite coating at this concentration had the best corrosion resistance, which was consistent with the previous potentiodynamic polarization curve test results. The corrosion resistance test results showed that the Gr/Ni-3 composite coating had excellent corrosion resistance, which provided effective protection for AZ91D magnesium alloy in Cl^- environment.

3.5 Graphene and multi-interface synergetic sandwich-like Gr/Ni composite coating

Multi-layer structure of coatings has received extensive attention for their excellent interfacial effects. In particular, the multi-layer passive film design could delay the anti-corrosion time, thereby achieving a long-term corrosion resistance effect for coating. Herein, we introduced the concept of multi-interface design combined with graphene modification for constructed Ni-based coating. The above discussion confirmed that the Gr/Ni-3 composite coating electroplated with a graphene doping concentration of 0.2 g/L could possess the best performance. Finally, the paper was researched that the optimal Gr/Ni-3 composite coating was used to combine with the synergetic multi-interface structure so as to construct a sandwich-like Gr/Ni composite coating on the surface of AZ91D magnesium alloy. And, the

kind of novel composite coating was also characterized in detail. In particular, by utilizing the first-principles calculations, we successfully explained the agglomeration mechanism of graphene during the reduction process of graphene oxide. At the same time, the reason why graphene preventing from Cl^- penetrating into coating was explained from the perspective of adsorption energy.

3.5.1 Microstructure of sandwich-like Gr/Ni composite coating

As shown in Fig. 16 (a) and (b), the surface of sandwich-like Gr/Ni composite coating exhibits the highest roughness (70.11 nm) and grain refinement features. The cross-sectional morphology (Fig. 16 (c)) of the coating showed an obvious multilayer structure inside the coating. The C element in the line scan of the cross-section showed overlapping features, and these results indicated that the multilayer structure was successfully deposited on the surface of the magnesium alloy. The grain size of the composite coating was calculated to be 89 nm by means of XRD (Fig. 16(d)) analysis, which indicates that the multi-layer structure was beneficial to reduce the grain size. It may be because the high roughness of the transition layer provides more intercalation points for the graphene sheets, thereby enhancing the micro-nano electrode effect and causing the grain refinement phenomenon inside the coating. Raman test (Fig. 16(e)) found that all characteristic peaks of graphene with the multilayer coating were intact, and the I_D/I_G dropped to 0.92. The results indicated that the multilayer structure reduced the agglomeration and structural defects of graphene in the coating. The micro-nano electrode effect of graphene would preferentially attract nickel ions to form reduction on the surface. Fig. 16(f) was the XPS spectra of the surface of the composite coating. The sp^2 C-C bond content indicates the reduction of residual oxygen radicals in graphene [24-28]. From the surface information of the bilayer

composite coating, it could be found that the multi-layer design was beneficial to reduce the grain size inside the coating and optimize the graphene structure.

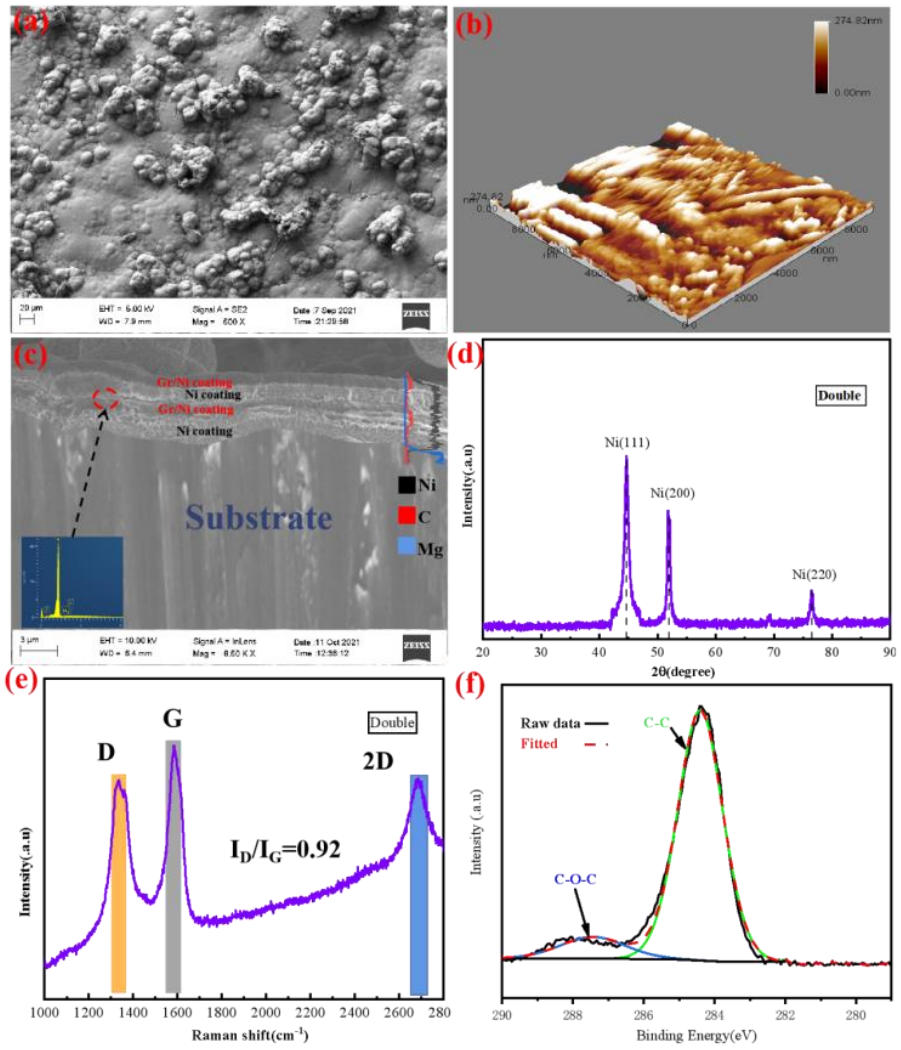

Fig. 16. Morphology of double-layered Gr/Ni composite coating: surface SEM image (a), AFM (b) , cross-section SEM (c), XRD (d), Raman (e) , XPS (f).

3.5.2 The performances of sandwich-like Gr/Ni composite coating

Compared with single-layered Gr/Ni-3 coating, the water contact angle of sandwich-like Gr/Ni composite coating was increased by 5°, the microhardness increased 275 HV, and the critical load increased to 63.18 N. It indicated that the multi-layer structure effectively improves the hydrophobicity and wear resistance of the coating. The phenomenon was

mainly because the multi-layer structure effectively reduces graphene defects and improves the hydrophobic properties of the coating, and the multi-layer can reduce the grain size and improve the hardness of the coating.

Fig. 17 (a-c) showed the relevant information after the friction test of the sandwich-like Gr/Ni composite coating in different environments. In atmospheric and seawater environments, the friction coefficient of sandwich-like Gr/Ni composite coating was lower than Gr/Ni-3 sample. It was mainly because the multilayer structure can provide more adsorption sites for grain nucleation, thus facilitating grain refinement. In particular, the multi-layer structure can effectively reduce the internal stress inside the coating and provide more deformation micro-regions for the coating, thereby improving its plastic deformation resistance.

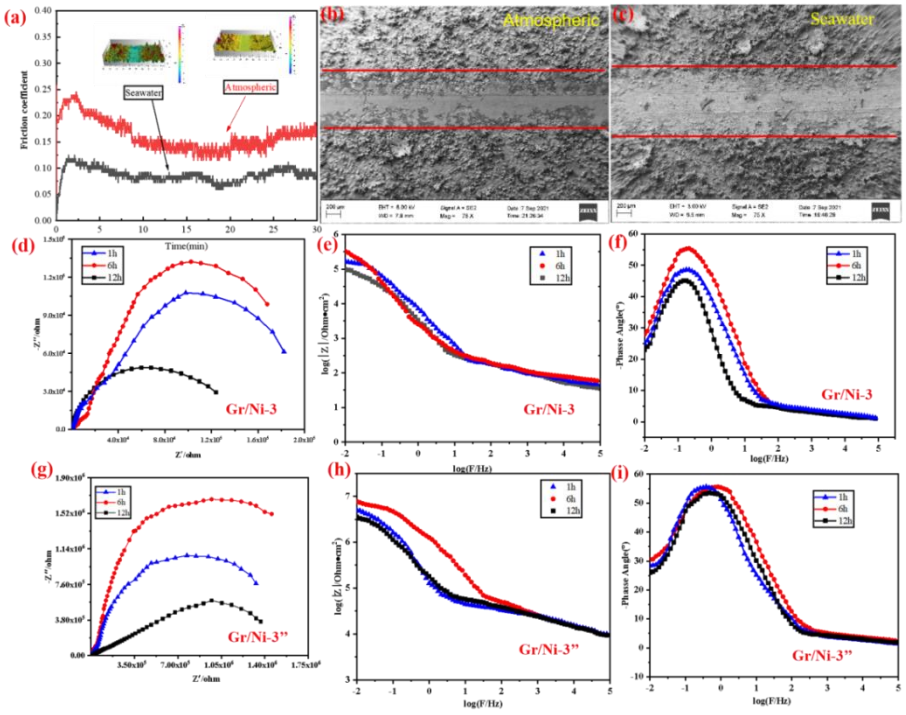

Fig. 17. (a)Friction coefficient of double-layered Gr/Ni composite coating in different environments; (b)SEM images of wear tracks in the atmosphere; (c)SEM images of wear tracks in the seawater; (d-f)Long-term electrochemical information of double-layered Gr/Ni composite coating; (g-i)long-term electrochemical information .

The corrosion potential and corrosion current of double-layered Gr/Ni composite coating was -0.05V and 0.071 μA/cm^2, respectively. Compared with Gr/Ni-3 (-0.14 V, 0.32 μA/cm^2), sandwich-like Gr/Ni composite coating exhibits more positive corrosion potential and lower corrosion current. The results indicated that the corrosion resistance of sandwich-like Gr/Ni composite coating is better than Gr/Ni-3 sample. The two composite coatings were soaked in 3.5 wt.% NaCl solution for different time periods. Fig. 17 (d-i) shows the associated EIS, impedance modulus and phase angle plots. The results showed that the long-term corrosion resistance of sandwich-like Gr/Ni composite coating is much better than Gr/Ni-3 sample. First, the high hydrophobicity of the double-layer composite coating prolongs the intrusion time of the corrosive medium, which is beneficial to its long-term corrosion resistance. Secondly, the anti-adsorption of Cl^- by graphene flakes reduces the intrusion of Cl^- into the coating, thus achieving corrosion resistance. Above all, the layer-by-layer passivation film effect brought by the multi-layer structure, thus repeatedly preventing the corrosive medium from invading the coating, and finally achieving a long-term corrosion resistance effect. In summary, the sandwich-like Gr/Ni composite coating has the best corrosion resistance, which helps to extend its service life in salt spray environment.

3.5.3 Simulation calculations for sandwich-like Gr/Ni composite coating

As shown in Fig. 18, we simulated the schematic diagram (a) of Ni adsorption at different positions on the graphene surface, and calculating the system free energy change (b) at the adsorption sites. From the change of free energy, it can be found that the free energy of the Ni adsorption bridge site is the lowest [29,30], and the adsorption energy of this model is calculated to be 1.82 eV. The DFT calculation results show that there is a sequential adsorption sequence in the process of nickel

deposition on the micro-nano electrode (graphene sheet), and the nickel atom and the bridge site forms a stable adsorption structure. When nickel atoms occupy the bridge site, nickel will gradually transfer to the secondary adsorption point. The nickel deposition process promotes the folded structure of the graphene sheet, which keeps the graphene sheet in a state with the lowest total free energy. This explains the irreversible agglomeration feature generation mechanism of graphite sheets during the reduction process.

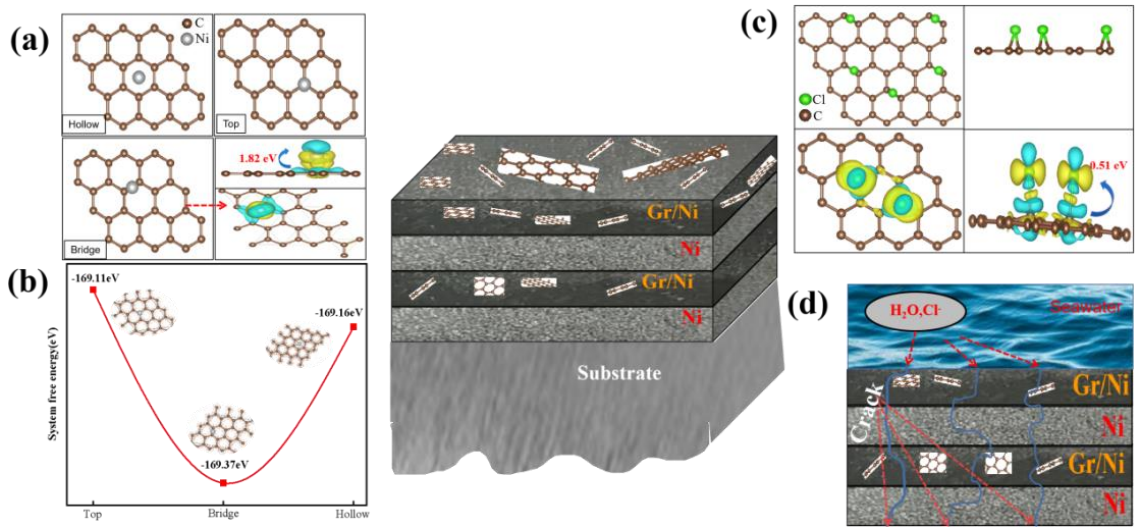

Fig. 18. Simulation calculations for double-layered Gr/Ni composite coating: Ni adsorption model (a); system Free Energy of Ni Adsorption (b); adsorption energy of Cl (c); schematic diagram of graphene and multi-interface synergetic design (d).

With the help of DFT, we further analyze why graphene could prevent Cl ions from eroding the composite coating. The adsorption energy (Fig. 18 (c)) of graphene sheet for Cl was 0.51 eV, indicated that graphene does not form a stable adsorption structure with Cl. In the seawater environment, the intrusion of Cl could exacerbate the generation of electrochemical corrosion. The lower the defect of graphene, the weaker the adsorption of Cl^-; and the low defect would help to prevent the corrosion medium from penetrating the graphene surface [30-32]. In

previous tests, we found that the multilayer structure can reduce the defects of graphene, which is beneficial to prevent the intrusion of corrosive media such as Cl^-. Therefore, the sandwich-like Gr/Ni composite coating exhibits excellent corrosion and wear properties in marine environments. In conclusion, the sandwich-like Gr/Ni composite coating prepared with the multilayer structure exhibits better wear resistance than the single-layer composite coating in aviation and deep-sea environments.

The protective effect of the multilayer interface is shown in Fig. 18 (d). Compared with the single-layer coating, the internal corrosion channel of the sandwich-like Gr/Ni composite coating is more tortuous, thereby delaying the intrusion time of the corrosion solution. In addition, during the corrosion process, a large number of micro etching substances will be formed on the surface of the coating to block the medium channels, thereby forming a passivation film. The layer-by-layer damage of the layers will continue to intensify this process, which will eventually manifest as a longer corrosion resistance time. Therefore, the multi-layer structure can effectively enhance the corrosion resistance of the graphene/nickel composite coating, which provides a preparation idea for its use in a salt spray environment.

4. Conclusion

Series of Gr/Ni composite and the sandwich-like Gr/Ni composite coating were prepared on AZ91D magnesium alloy by electroplating technology, and their microstructure, mechanical and corrosion performances were systematically investigated. Particularly, DFT calculation was used to explore the effective mechanism of graphene and multi-interface synergism for sandwich-like Gr/Ni composite coating. The following conclusions are drawn below:

1) The grain size of as-plated Gr/Ni composite firstly decreased and then increased as increasing graphene concentration in the electroplating. When the doping concentration of graphene was 0.2 g/L, the grain size of as-plating Gr/Ni-3 composite coating was the smallest.

2) Graphene was beneficial to improve the corrosion and wear resistance of Gr/Ni composite coatings. However, too high doping graphene into Gr/Ni composite coating would aggravate the wear degree due to reducing the hardness of the coating. Therefore, the optimal graphene doped into Gr/Ni composite coating could result in superior anti-corrosion and anti-wear abilities in marine environment.

3) In particular, the sandwich-like Gr/Ni composite coating exhibited excellent long-term corrosion resistance compared to single-layered Gr/Ni composite. It came from the multi-interfacial passivation film mechanism brought by the multi-layer design, which greatly delays the time for the corrosive medium to invade the substrate.

4) DFT calculations revealed that the adsorption of nickel to graphene exhibits sequential adsorption characteristics, nickel was preferentially adsorbed on the bridge sites of graphene, and gradually adsorbed on secondary adsorption sites. Those actions could result in the agglomeration of graphene sheets in the electroplating. However, the multi-interface could provide more stretching space for graphene sheets and reduce the folding tendency of graphene. As a result, the sandwich-like Gr/Ni composite coating exhibited the most excellent properties, which provided feasible way to protect AZ91D magnesium alloy so as to enhance its services in marine and aviation environments.

Acknowledgements

This work was supported by funding from the National Natural Science Foundation of China (Grant No. 52065025) and The Youth Jinggang Scholars Program in Jiangxi Province.

References

[1] Y. Zhou, P. Zhang, F. Yan, Corrosion resistance of a nano-Mg modified silane conversion coating with cathodic protection on magnesium alloy AZ91D. Materials Letters, 284 (2021) 128930.

[2] F. Yan, B. Chen, J. Yao, D. Zhang, M. Yan, Y. Zhang, Characterization of microstructure and corrosion properties of AZ91D magnesium alloy surface-treated by coating-nitriding. Journal of Materials Research and Technology, 14 (2021) 1559-1568.

[3] F. Wen, J. Zhao, M. Yuan, J. Wang, D. Zheng, J. Zhang, Y. Guo, Influence of Ni interlayer on interfacial microstructure and mechanical properties of Ti-6Al-4V/AZ91D bimetals fabricated by a solid–liquid compound casting process. Journal of Magnesium and Alloys, 9 (2021) 1382-1395.

[4] G. Li, W. Jiang, F. Guan, J. Zhu, Y. Yu, Z. Fan, Improving mechanical properties of AZ91D magnesium/A356 aluminum bimetal prepared by compound casting via a high velocity oxygen fuel sprayed Ni coating. Journal of Magnesium and Alloys, 10 (2022) 1075-1085.

[5] J. Zhu, H. Jia, K. Liao, X. Li, Improvement on corrosion resistance of micro-arc oxidized AZ91D magnesium alloy by a pore-sealing coating. Journal of Alloys and Compounds, 889 (2021) 161460.

[6] L. Ji, F. Chen, H. Huang, X. Sun, Y. Yan, X. Tang, Preparation of nickel–graphene composites by jet electrodeposition and the influence of graphene oxide concentration on the morphologies and properties. Surface and Coatings Technology, 351 (2018) 212-219.

[7] H. Zhang, N. Zhang, F. Fang, Synergistic effect of surfactant and saccharin on dispersion and crystal refinement for electrodeposition of nanocrystalline nickel/graphene oxide composite. Surface and Coatings Technology, 402 (2020) 126292.

[8] W. Shang, F. Wu, Y. Wen, C. He, X. Zhan, Y. Li, Corrosion resistance and mechanism of graphene oxide composite coatings on magnesium alloy. Industrial & Engineering Chemistry Research, 58(3) (2018) 1200-1211.

[9] O.Y. Kurapova, I.V. Lomakin, S.N. Sergeev, E.N. Solovyeva, A.P. Zhilyaev, I.Y. Archakov, V.G. Konakov, Fabrication of nickel-graphene composites with superior hardness. Journal of Alloys and Compounds, 835 (2020) 155463.

[10] R. Askarnia, B. Ghasemi, S.R. Fardi, E. Adabifiroozjaei, Improvement of tribological, mechanical and chemical properties of Mg alloy (AZ91D) by electrophoretic deposition of alumina/GO coating. Surface and Coatings Technology, 403 (2020) 126410.

[11] P. Bagalà, F.R. Lamastra, S. Kaciulis, A. Mezzi, G. Montesperelli, Ceria/stannate multilayer coatings on AZ91D Mg alloy. Surface and Coatings Technology, 206 (2012) 4855-4863.

[12] D. Zhang, Z. Qi, B. Wei, Z. Wu, Z. Wang, Anticorrosive yet conductive Hf/Si3N4 multilayer coatings on AZ91D magnesium alloy by magnetron sputtering. Surface and Coatings Technology, *309* (2017) 12-20.

[13] G. Kresse, J. Furthmüller, Efficient iterative schemes for ab initio total-energy calculations using a plane-wave basis set. Physical review B, 54 (1996) 11169.
[14] G. Kresse, J. Furthmüller, Efficiency of ab-initio total energy calculations for metals and semiconductors using a plane-wave basis set. Computational materials science, 6 (1996) 15-50.
[15] G. Yasin, M. Arif, M. Shakeel, Y. Dun, Y. Zuo, W.Q. Khan, M. Nadeem, Exploring the nickel-graphene nanocomposite coatings for superior corrosion resistance: manipulating the effect of deposition current density on its morphology, mechanical properties, and erosion-corrosion performance. Advanced Engineering Materials, 20 (2018) 1701166.
[16] Y. Wu, H. Luo, H. Wang, L. Zhang, P. Liu, L. Feng, Fast adsorption of nickel ions by porous graphene oxide/sawdust composite and reuse for phenol degradation from aqueous solutions. Journal of colloid and interface science, 436 (2014) 90-98.
[17] D. Kuang, L. Xu, L. Liu, W. Hu, Y. Wu, Graphene–nickel composites. Applied Surface Science, 273 (2013) 484-490.
[18] H. Zhang, Z. Nan, F. Fang, Fabrication of high-performance nickel/graphene oxide composite coatings using ultrasonic-assisted electrodeposition. Ultrasonics sonochemistry 62 (2020) 104858.
[19] M. Hilder, B. Winther-Jensen, D. Li, M. Forsyth, D.R. MacFarlane, Direct electro-deposition of graphene from aqueous suspensions. Physical Chemistry Chemical Physics, 13 (2011) 9187-9193.
[20] D.K. Owens, R.C. Wendt, Estimation of the surface free energy of polymers. Journal of applied polymer science, 13 (1969) 1741-1747.
[21] N.W. Robert, Resistance of solid surfaces to wetting by water. Industrial & Engineering Chemistry, 28 (1936) 988-994.
[22] R. Raj, S.C. Maroo, E.N. Wang, Wettability of graphene. Nano letters, 13 (2013) 1509-1515.
[23] J. Jiang, C. Feng, W. Qian, L. Zhu, S. Han, H. Lin, Effect of graphene oxide nanosheets and ultrasonic electrodeposition technique on Ni‑Mo/graphene oxide composite coatings. Materials Chemistry and Physics, 199 (2017) 239-248.
[24] H. Yue, L. Yao, X. Gao, S. Zhang, E. Guo, H. Zhang, B. Wang, Effect of ball-milling and graphene contents on the mechanical properties and fracture mechanisms of graphene nanosheets reinforced copper matrix composites. Journal of Alloys and Compounds, 691 (2017) 755-762.
[25] W. Yao, Y. Chen, L. Wu, J. Zhang, F. Pan, Effective corrosion and wear protection of slippery liquid-infused porous surface on AZ31 Mg alloy. Surface and Coatings Technology, 429 (2022) 127953.
[26] S.H. Tsai, J.G. Duh, Microstructure and mechanical properties of CrAlN/SiNx nanostructure multilayered coatings. Thin Solid Films, 518 (2009) 1480-1483.
[27] P. Li, L. Chen, S.Q. Wang, B.Yang, Y. Du, J. Li, M.J. Wu, Microstructure, mechanical and thermal properties of TiAlN/CrAlN multilayer coatings. International Journal of Refractory Metals and Hard Materials, 40 (2013) 51-57.
[28] Z. Shi, M. Liu, A. Atrens, Measurement of the corrosion rate of magnesium alloys using Tafel extrapolation. Corrosion science, 52 (2010) 579-588.
[29] S. J. An, Y. Zhu, S.H. Lee, M.D. Stoller, T. Emilsson, S. Park, R.S. Ruoff, Thin film fabrication and simultaneous anodic reduction of deposited graphene oxide platelets by electrophoretic deposition. The Journal of Physical Chemistry Letters, 1 (2010) 1259-1263.
[30] G. Greczynski, L. Hultman, X-ray photoelectron spectroscopy: towards reliable binding energy referencing. Progress in Materials Science, 107 (2020) 100591.

[31] M. Wang, L. Ma, H. Chen, S. Zhou, Z. Lu, C. Hou, First-principles calculations to explore the oxygen effects on WS_2 film in marine environments. Applied Surface Science, 566 (2021) 150741.
[32] S. Zhou, W. Yao, Z. Wang, L. Ma, Z. Lu, C. Hou, The first-principles calculations to explore the mechanism of oxygen diffusion on vacancy defective graphene in marine environment. Applied Surface Science, 525 (2020) 146585.